

# Systematic Simulation-Based Predictive Synthesis of Integrated Optical Interconnect

Ian O'Connor, *Member, IEEE*, Faress Tissafi-Drissi, Frédéric Gaffiot, Joni Dambre, *Member, IEEE*, Michiel De Wilde, Joris Van Campenhout, *Student Member, IEEE*, Dries Van Thourhout, *Member, IEEE*, Jan Van Campenhout, *Member, IEEE*, Dirk Stroobandt, *Member, IEEE*

**Abstract**—Integrated optical interconnect has been identified by the ITRS as a potential solution to overcome predicted interconnect limitations in future systems on chip. However, the multi-physics nature of the design problem and the lack of a mature integrated photonic technology have contributed to severe difficulties in assessing its suitability. This paper describes a systematic, fully automated synthesis method for integrated microsource-based optical interconnect capable of optimally sizing the interface circuits based on system specifications, CMOS technology data and optical device characteristics. The simulation-based nature of the design method means that its results are relatively accurate, even though the generation of each data point requires only 5 minutes on a 1.3 GHz processor. This method has been used to extract typical performance metrics (delay, power, interconnect density) for optical interconnect of length 2.5mm-20mm in three predictive technologies at 65nm, 45nm and 32nm gate length.

**Index Terms**—integrated optical interconnect, multi-domain design methods, synthesis

## I. INTRODUCTION

THE emergence of very high performance systems on chip (SoC) is necessary to achieve future required application performance in terms of resolution (audio, video and computing) and CPU power / total MIPS (real-time encoding-decoding, data encryption-decryption). The shift to distributed multi-processor architectures is the recognized route to such performance and therefore requires organized high-speed communication between processors. Metallic interconnect will be highly inefficient in this role due to unachievable tradeoffs between design parameters (the main limitations due to metallic interconnects are inter-line crosstalk, latency, global throughput, connectivity and power consumption).

Manuscript received XXXXXX. This work was supported by the European FP6 IST program under PICMOS FP6-2002-IST-1-002131.

Ian O'Connor and Frédéric Gaffiot are with Ecole Centrale de Lyon, Ecully, France (corresponding author Ian O'Connor - phone: +33 472 186054; fax: +33 478 433593; e-mail: ian.oconnor@ec-lyon.fr).

Faress Tissafi-Drissi was with Ecole Centrale de Lyon, Ecully, France, and is now with Dolphin Integration, Meylan, France.

Joni Dambre, Michiel De Wilde, Jan Van Campenhout and Dirk Stroobandt are with Ghent University, Belgium, Electronics and Information Systems Department; Joris Van Campenhout and Dries Van Thourhout are with Ghent University, Belgium, INTEC department

It is believed that the concept of integrated optical interconnect is a potential technological solution to alleviate some of these issues involved in exchanging data between cores in SoC architectures. However, the multi-physics nature of the design problem and the lack of a mature integrated photonic technology have contributed to severe difficulties in assessing the suitability of integrated optical interconnect for on-chip data transport. In turn, these difficulties have rendered unclear the research directions for the integrated photonic device community. The objective of optical interconnect assessment should thus be two-fold: firstly, to explore the performance capabilities of optical links with existing technological constraints; and secondly, to provide feedback to be taken into account in component and integration oriented research.

To enable the analysis described above, it is necessary to define and quantify the specification set for the various subcomponents in an integrated optical link. This requires the development of models and tools to design and optimize optical interconnect in a range of technologies and under a range of specification conditions, in order to evaluate the properties of the technologies developed. Ultimately, the objective is to compare them to the performance of current and future electrical interconnect alternatives in terms of important performance metrics (mainly area, data rate and power). A contiguous aim is to determine the specifications for which the proposed technologies would outperform traditional interconnect.

Optical-electrical interconnection comparison is not new: several authors have already published comparative studies between optical and electrical on-chip interconnect technologies [1][2][3]. Most of those consider expected technological evolutions to provide a roadmap of interconnect performance. This is done either by using analytical models, or by a simulation-based approach. Analytical models are usually based on ITRS<sup>1</sup> [4] or other expected future CMOS technology parameters and rough estimates of optical interconnect performance. Simulation models are either self-constructed, based on ITRS parameters, or using publicly available Predictive Technology Models (PTM - now available<sup>2</sup> for gate lengths ranging down to 32nm).

<sup>1</sup> International Technology Roadmap for Semiconductors (<http://public.itrs.net>)

<sup>2</sup> <http://www.eas.asu.edu/~ptm/>

In this work, as it was intended to be able to determine device-level specifications, it was necessary to generate accurate optical link performance estimates that can be traced back to individual component parameters. Part of the optical link consists of analog CMOS circuitry. The design thereof can be done based on analytical models, but it is very sensitive to MOSFET parasitics so it is crucial that these parameters are available. However, the data presented in the ITRS is intended for digital design applications. This implies that estimates on transistor parasitics are very rough or in some cases not even available. Hence, for an accurate evaluation, it is best to use technologies for which simulation models are available.

For these reasons we have developed a simulation-based approach for optical interconnect synthesis. By way of illustration, we apply our approach to predictive technology models with gate lengths of 65nm, 45nm and 32nm. In contrast to the model based approaches, our choice implies that we presently cannot stretch our analysis beyond 32nm gate lengths according to the availability of models. However, according to the ITRS, a 32nm gate length technology (which is the smallest available transistor model on the PTM website) would be taken into production for high-end applications in 2008, and this is only the beginning of its lifetime. Therefore we claim that our analysis does stretch sufficiently far into the future. Also, by extrapolating observed trends in performance metric evolution over technology nodes, some insight into the possible results for future technology nodes can be obtained.

The models and software developed were therefore made to be sufficiently generic in order to enable the exploration of a) performance capabilities of optical links with existing technological constraints; and b) the impact of improvements in device performance on interface circuit sizing and overall link performance. This set of data allows tradeoffs to be understood, as well as their relevance in the context of overall link performance metrics.

This paper firstly describes some technological and device aspects in section II. The generation of optical link parameters based on link specifications is based on analog synthesis techniques, and the individual interface circuit synthesis methods are described in section III. To enable complete optical link simulation, a number of behavioral models were developed, and this work is outlined in section IV, although details are outside the scope of this paper. Section V concentrates on describing the complete optical link synthesis method exploiting the simulation work and individual circuit synthesis methods, as well as the details of the investigation program. Extraction methods concerning interconnect density analyses are described in section VI. To generate performance metric data for considered technologies and optical link lengths, the simulation-based quantitative assessment of optical interconnects at the physical link level is described in section VII. Through identification of the impact of individual device parameter variations on particular performance metrics, an exploration of these variations is shown in section VIII.

## II. TECHNOLOGY AND DEVICE ASPECTS

Various technological solutions exist for using optics with a standard CMOS SoC [5]. Our approach is generic, in the sense that it can be applied to any type of integrated photonic technology, as long as a behavioral model is available for each component (section IV). In this work we have supposed a microsource-based link using heterogeneous integration [6] to achieve an above-IC optical transport layer (Figure 1). A CMOS driver circuit modulates the current flowing through the microsource laser, and thus the intensity of light emission. The microsource is coupled to a passive waveguide structure and provides a signal to an optical receiver (or possibly to several, as in the case of a broadcast function). At the receiver, the high-speed optical signal is converted back to an electrical digital (rail to rail) signal and subsequently distributed by a local electrical interconnect network, represented by an output capacitance (fanout) that the link can drive. Similarly, the overall input capacitance presented by the link to the digital signal generator is part of the specification set for the optical link.

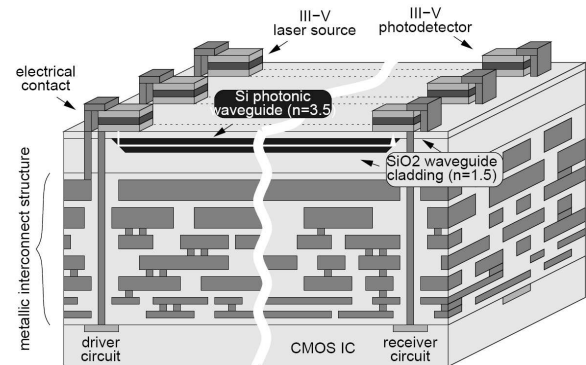


Figure 1 Cross section of optical interconnect structure

To form a planar optical waveguide, the most common CMOS-compatible materials used are polymers,  $\text{Si}_3\text{N}_4$  and silicon. In a first approach, we assumed silicon as the core and  $\text{SiO}_2$  as the cladding material.  $\text{Si}/\text{SiO}_2$  structures are compatible with conventional silicon technology and are transparent for 1.3-1.55 $\mu\text{m}$  wavelengths. Such waveguides also benefit from a high relative refractive index difference  $\Delta \approx (n_1^2 - n_2^2)/2n_1^2$  between the core ( $n_1 \approx 3.5$  for Si) and claddings ( $n_2 \approx 1.5$  for  $\text{SiO}_2$ ) and enable the realization of compact optical circuits, with bend radius of the order of a few  $\mu\text{m}$  [7] and low pitch to crosstalk ratio. To avoid modal dispersion, improve coupling efficiency and reduce loss, single mode conditions are applied to the waveguide dimensions. For a wavelength of 1.55 $\mu\text{m}$  in  $\text{Si}/\text{SiO}_2$ , the waveguide dimensions are around 0.5 $\mu\text{m}$  x 0.22 $\mu\text{m}$  (width x height).

$\text{Si}_3\text{N}_4$  waveguides are also contenders for optical interconnect. Since the index difference is lower, the propagation delay is also lower, but the penalty for this is higher crosstalk and bend loss, which implies a requirement for higher pitch and limited use of bends. The waveguide dimensions for these waveguides are around 0.4 $\mu\text{m}$  x 0.8 $\mu\text{m}$

(width x height). Data for both types of waveguide is given in the optical link simulation section IV.

Integrated III-V sources can achieve >10GHz 20% total efficiency (including coupling to waveguide) when biased above a 40 $\mu$ A threshold current, and have a footprint of some 10x10 $\mu$ m<sup>2</sup> [8]. Similarly, 50 $\mu$ m<sup>2</sup> InP detectors exhibit 24GHz 70% responsivity and low (<10fF) capacitance [9]. Heterogeneous integration/bonding of such devices on CMOS has also been proven [10].

### III. SYNTHESIZABLE MODEL LIBRARY

Manual design of physically heterogeneous systems results in long design cycles and increasingly apparent bottlenecks in the overall design process [11]. This explains the growing awareness in industry that the advent of heterogeneous synthesis and optimization tools is a necessary step to increase design productivity by assisting or even automating the design process. The fundamental goal of heterogeneous synthesis is to quickly generate a first-time-correct sized schematic from a set of specifications. This is critical since the heterogeneous design problem is typically under-constrained with many degrees of freedom and with many interdependent (and often-conflicting) performance requirements to be taken into account across physical domains. For this work, this type of approach is essential since the objective is to explore the design of optical links subject to many sets of performance requirements and to many sets of technological and device-level constraints.

For this work we used our synthesis framework RuneII [12], which enables the specification and automated design of heterogeneous systems, using a hierarchical approach to partition the system at a behavioral description level, and domain-specific simulators to design individual blocks. It exploits the concept of synthesizable AMS IP [13], which extends the concept of digital and software IP to the analog and heterogeneous domains. In essence, all information necessary for the design of a given block is formalized in a technology-independent way such that a generic framework (such as RuneII) can exploit the various facets of the AMS IP information to arrive at a sized system schematic satisfying all performance requirements in the target technology.

To carry out a systematic design analysis of optical interconnects, a set of design requirements and synthesizable models must be established. This section will detail the various synthesizable models developed (their final integration into a complete optical link synthesis method will be described in section V).

#### A. Receiver circuit synthesizable model

The classical structure for a receiver circuit is shown in Figure 2: a transimpedance amplifier (TIA) converts the photocurrent of a few  $\mu$ A into a voltage of a few mV; a comparator generates a rail-to-rail signal; and a data recovery circuit eliminates jitter from the restored signal.

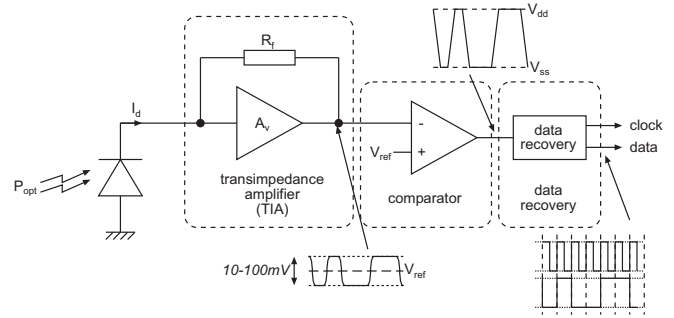


Figure 2 Typical receiver circuit structure

Of these, the TIA is arguably the most critical component, since it has to cope with a generally large photodiode capacitance situated at its input. For the comparator, scaling figures were used from a reference circuit manually designed at the 90nm gate length node, and the input capacitance estimated for TIA synthesis.

It should be noted that photodetector capacitances in advanced devices can be around 10fF or less – at this level, it is likely that the input capacitance of the TIA itself will play a large part in the determination of bandwidth. Bandwidth/power ratio maximization can be achieved in several ways:

- parametric optimization: for a given transimpedance structure, find the combination of component parameters necessary for maximum bandwidth
- structural modification: for a given preamplifier architecture, make structural modifications, usually by adding elements such as inductors for shunt peaking [14] or capacitors as artificial loads or feedback [15]
- architectural exploration: use complex architectures such as bootstrap or common-gate input stages [16]

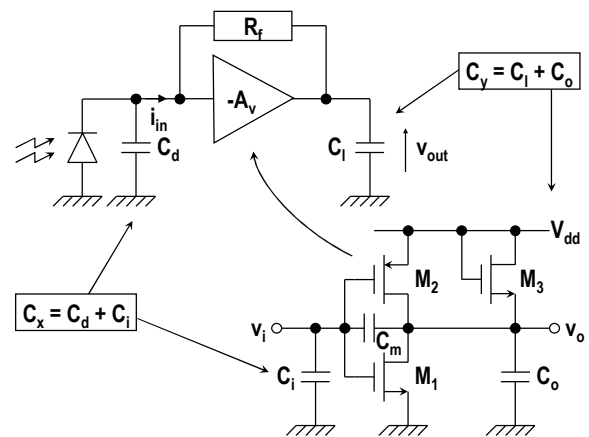


Figure 3 Resistive feedback transimpedance amplifier and CMOS fast inverter structure used as internal amplifier in TIA

The basic transimpedance amplifier structure in a typical configuration is shown in Figure 3, with the internal structure of the amplifier used in the resistive feedback configuration [17]. In the following analysis,  $C_x$  represents the aggregated capacitance at the TIA input node (including the photodetector

capacitance  $C_d$ ),  $C_y$  represents the aggregated capacitance at the TIA output node (including the load capacitance  $C_l$ ),  $C_m$  represents the aggregated Miller capacitance between the TIA input and output nodes,  $R_f$  represents the feedback resistance value,  $R_o$  represents the fast inverter output resistance and  $A_v$  represents the fast inverter voltage gain. The bandwidth/power ratio of this structure can be maximized by using small-signal analysis and mapping of the individual component values to a filter approximation of Butterworth type, which gives:

$$Z_{g0} = \frac{R_o - R_f A_v}{1 + A_v} \quad (1)$$

$$\omega_0 = \frac{1}{R_o C_y} \sqrt{\frac{1 + A_v}{M_f (M_x + M_m + M_x M_m)}} \quad (2)$$

$$Q = \frac{\sqrt{M_f (M_x + M_m (1 + M_x)) (1 + A_v)}}{1 + M_x (1 + M_f) + M_m M_f (1 + A_v)} \quad (3)$$

where the multiplying factors  $M_f = R_f / R_o$ ,  $M_i = C_x / C_y$  and  $M_m = C_m / C_y$  are introduced, normalizing all expressions to the time constant  $\tau = R_o C_y$ . By rearranging these equations, it is then possible to develop a synthesis procedure which, from desired transimpedance performance criteria ( $Z_{g0}$ , bandwidth and  $Q$ ) and operating conditions ( $C_d$ ,  $C_l$ ) generates component values for the feedback resistance  $R_f$  and the voltage amplifier ( $A_v$  and  $R_o$ ).

Taking into consideration their physical realization, amplifiers with requirements for low gain and high output resistance (high  $R_o / A_v$  ratio) are the easiest to build, and also require the least quiescent current and area. Figure 4 shows a plot of this quantity against the TIA specifications (bandwidth and transimpedance gain) for  $C_x = C_d = 400\text{fF}$  and  $C_y = C_l = 100\text{fF}$ .

Approximate equations for the small-signal characteristics and bias conditions of the circuit allow a first-cut sizing of the amplifier. The solution is then fine-tuned by a local numerical optimization method driven by a sum of weighted cost functions to achieve the desired values of  $A_v$  and  $R_o$ , using simulation for exact results [18]. Parasitic capacitances are extracted from the resulting transistor sizes and are used to update the values of  $C_x$  and  $C_y$ . The transimpedance amplifier sizing and amplifier optimization steps are subsequently run again with continually updating values of  $A_v$ ,  $R_o$ ,  $C_x$  and  $C_y$  until the process converges.

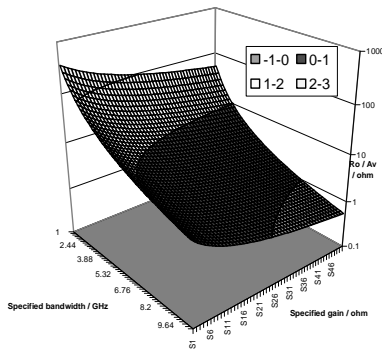


Figure 4  $R_o/A_v$  design space with varying bandwidth and transimpedance gain requirements

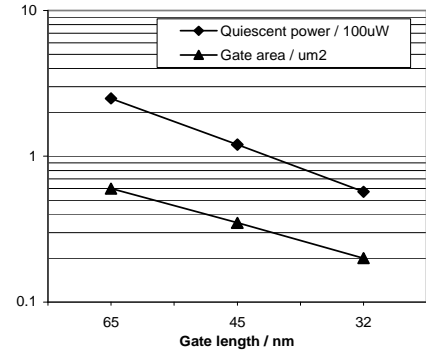


Figure 5 Evolution of TIA characteristics (power, area, noise) with technology node for  $Z_{g0} \cdot BW = 1\text{THz}\Omega$ ,  $C_d = 400\text{fF}$ ,  $C_l = 45\text{fF}$

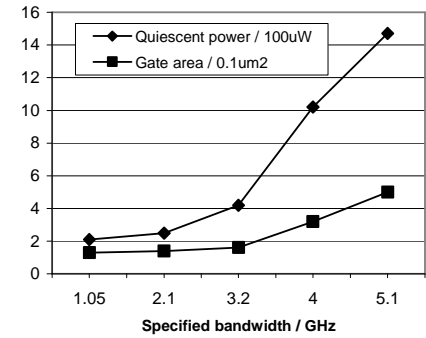


Figure 6 Power and area against bandwidth requirement for TIAs at the 65nm technology node for  $L_g = 65\text{nm}$ ,  $C_d = 400\text{fF}$ ,  $C_l = 45\text{fF}$

Using this methodology and predictive BSIM3v3 and BSIM4 models for technology nodes from 65nm down to 32nm, we generated design parameters for 1THz $\Omega$  transimpedance amplifiers to evaluate the evolution in critical characteristics with technology node. Figure 5 shows the results of transistor level simulation of fully generated photo-receiver circuits at each technology node. According to traditional "shrink" predictions, which consider the effect of applying a unit-less scale factor of  $1/s$  to the geometry of MOS transistors, the quiescent power and device area should decrease by a factor of  $1/s^2$ . Between the considered technology nodes 65nm-32nm,  $s^2 = 4$ , which is approximately verified through the sizing procedure (quiescent power scales by  $1/4.4$ , gate area scales by  $1/3$ ). This methodology also allows us to find a particular specification to a given tolerance, as shown in Figure 6. This shows the active area and power of the generated TIA for bandwidths of 1GHz - 5GHz (with  $Z_{g0} = 1\text{k}\Omega$  and  $Q = 1/\sqrt{2}$  in the 45nm technology).

### B. Driver circuit synthesizable model

The basic current modulation configuration of the source driver circuit is shown in Figure 7. While more advanced driver schemes exist (such as voltage-pulsed drivers [19]), the current modulation circuit is sufficient to evaluate the characteristics of the overall link in a systematic way. The source is biased above its threshold current by  $M_2$  to eliminate

turn-on delays, and as the bias current value is the main contributing factor to emitter power, reducing the source threshold current is a primary device research objective (figures of the order of  $50\mu\text{A}$  appear achievable [8]). Device  $M_1$  modulates the current flowing through the source, and consequently the output optical power injected into the waveguide. The reduced dimensions of the microsource (with respect to commercial VCSELs) translate to lower parasitic capacitance and good bandwidth performance.

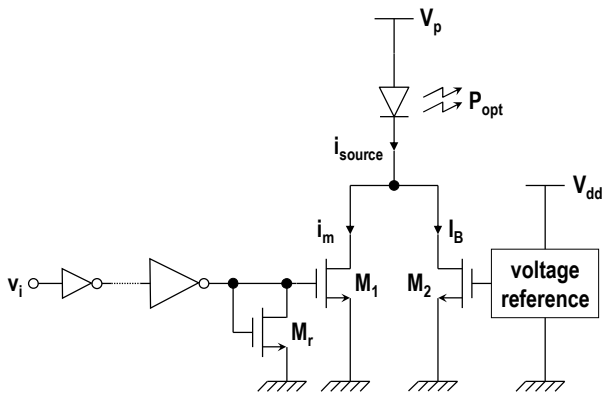


Figure 7 Basic current modulation source driver circuit

This circuit is sized simply by numerical bisection using the required values for the modulation current  $i_m$  and the bias current  $I_B$  (a unique solution exists).

#### IV. SIMULATION

To enable complete link simulation in an EDA framework, it is necessary to develop behavioral models for the optoelectronics devices and passive waveguides. For all behavioral models, the choice of an appropriate level of description is prerequisite to developing and using the models in the required context. Essentially, the description level falls into one of two categories: functional modeling or structural modeling. A functional model will describe the behavior of a device according to its specifications and behavioral equations, without defining the structure of the device. A structural model will describe the behavior of a device according to its internal structure and physical parameters, without necessarily satisfying the specification criteria (which do not have to be formalized in this approach).

Ideally, both functional and structural models should exist for the devices considered. However this is not absolutely necessary and careful consideration was given to choosing the appropriate description level for each device. Since the source behavior is arguably the most complex and likely to exhibit nonlinear behavior (thermal roll off, temperature changes) important to complete link simulation, it was decided to model this element at a structural level. The waveguide and detector were modeled at a functional level.

The models were all implemented in the OVI-96 Verilog-A subset of Verilog-AMS, an extension of the IEEE 1364-1995 Verilog hardware description language. This extension is an industry standard for analog simulation model description and

can be simulated with a number of general-purpose circuit simulators (we use Spectre<sup>TM</sup>). This way, the optical and photonic devices can be simulated together with the interface circuitry and with the rest of the optical link given adequate simulation models. This enables interesting optimization strategies (e.g., joint power optimization) and the analysis of link performance sensitivity to various parameter variations as well as temperature changes.

Detailed description of these models [20] is outside the scope of this paper, but the device parameters for optical interconnect varied in this analysis are shown in Table I, with minimum and maximum values defining the limits of the parameter variation. These limits are based on discussions with experts in the field [21], and on data available in the literature on sources [8], waveguides [7] and detectors [9]. The values in bold italic represent the (pessimistic) nominal values.

TABLE I  
OPTICAL DEVICE PARAMETERS

	Parameter	Min. value	Max. value	Units
Source	Total efficiency	<b>0.1</b>	0.3	mW/mA
	Area	10x10	<b>100x100</b>	$\mu\text{m}^2$
	Threshold current	1.5e-5	<b>1.5e-3</b>	A
	Bandwidth	10		GHz
Detector	Responsivity	<b>0.5</b>	0.7	mA/mW
	Area	10x10	<b>100x100</b>	$\mu\text{m}^2$
	Capacitance	1e-15	<b>1e-13</b>	F
	Dark current	1e-18		A
	Noise current	1e-15		A
	Bandwidth	20		GHz
Waveguide	Guide index	3.45	2.0	
	Cladding index	1.46	1.46	
	Height	0.22	0.8	$\mu\text{m}$
	Width	0.5	0.4	$\mu\text{m}$
	Pitch	1.1e-6	4e-6	m
	Loss	2.7	1.5	dB/cm
	Delay	13.3	6.7	ps/mm
	Excess bend loss	0.027	1.52	dB/90°
	Bend radius	2	10	$\mu\text{m}$

This enabling design technology was essential to carry out simulation in an EDA environment of the complete optical link, associating these behavioral models with transistor-level circuit schematics. The nonlinear behavior of the microsource laser was modeled (enabling visualization of physical limits) and converges systematically in Spectre. Achieving complete link simulation was a necessary step to enable subsequent simulation-based link synthesis (using interface circuit design variables) over a range of target technologies and specification sets to extract link performance data. The iterative optimization step is facilitated by the low simulation time required for the complete link (a few seconds for ten data bits on a 1.3GHz processor).

#### V. POINT-TO-POINT LINK SYNTHESIS

The objective of our work was to carry out transistor-level sizing of the receiver and of the driver circuits according to complete link specifications. The optical link under consideration is represented by Figure 8 (the CMOS structures used at transistor level are fixed in this synthesis procedure).

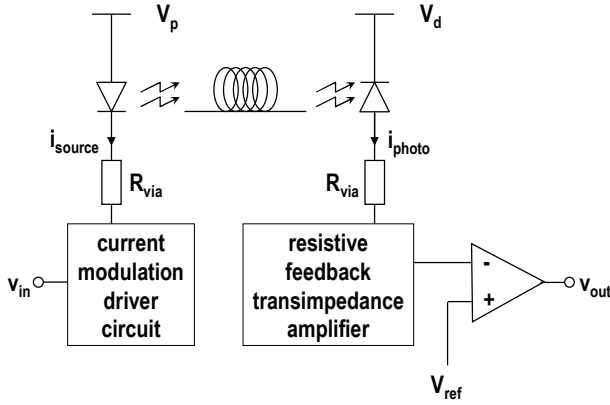


Figure 8 Optical link schematic

### A. Synthesis procedure

The synthesis approach implemented consists of creating scenarios allowing the specification of each model, evaluation and design methods, and of communication between the different blocks using synthesizable AMS IP. A device library containing the synthesizable models of each device in the optical link based on the UML language was developed to allow the modeling of this hierarchical synthesis problem. The procedure used to automatically synthesize an optical point-to-point link is shown in Figure 9.

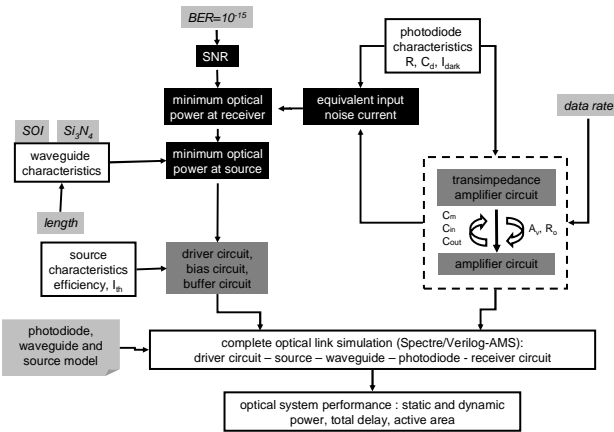


Figure 9 Optical link sizing method

The process starts by defining the photodetector characteristics and the required data rate. Using the method described in section III.A, the transistor-level schematic for the transimpedance amplifier is automatically generated and linked to a manually scaled comparator circuit.

The value of the rms noise power,  $i_n$ , is extracted from simulation of the schematic, and updated for each synthesis loop, using the Morikuni formula [19] in the transimpedance amplifier noise calculations:

$$i_n^2 = \left( 2q(I_{gate} + I_{dark}) + \frac{4kT}{R_f} \right) \frac{C}{4D} + 4kT \frac{C^2}{16\pi^2 DE} \frac{(2\pi C_T)^2}{g_m} \quad (4)$$

where

$$C = 1 + g_m R_f \quad (5)$$

$$D = R_o(C_x + C_y) + R_f(C_x + C_m) + g_m R_f R_o C_m$$

$$E = R_f R_o [(C_x + C_y)C_m + C_x C_y]$$

For a given BER (bit error rate) specification and noise signal associated with the photodiode and transimpedance circuit, we can then calculate the minimum optical signal power  $\Delta P_s$  required by the receiver to operate at the given error probability:

$$\Delta P_s = i_n \times SNR \quad (6)$$

where

$$SNR = (\text{erfc}^{-1}(2BER))^2 \quad (7)$$

Here SNR represents the linear signal to noise ratio (absolute value, not in dB). BER, defined as the rate of error occurrences, is one of the main criteria in evaluating the performance of digital transmission systems. In our analyses we fixed BER at  $10^{-18}$  bits<sup>-1</sup> (this corresponds to 1 error / 3.17 years for a single link at 10Gbps communication, or 1 error / 18 days for a 64-bit data bus at the same data rate.)

The value of the power which needs to be emitted by the laser source is evaluated from the calculated value of the minimum optical power at the receiver, and from the power losses induced by the waveguide structure (length and intrinsic loss, number of bends and loss/90° bend) and coupling. These figures depend to a large extent on the materials used.

The final sizing step is to calculate the driver and associated bias and buffer circuits using the emitted power value and the source characteristics in conjunction with the method described in section III.B. This then enables the simulation of the complete optical link, using transistor-level schematics for the interface circuits and behavioral models for the photonic devices. From the simulation results, the performance criteria can be extracted.

Using this approach, the synthesis problem is considered to be complete, such that no constraint partitioning is required. In fact, the constraints are derived directly from system specifications, and thus constraint exploration is achieved directly by the user, as shown in the investigation strategy detailed in section VII.

### B. Metrics

In order to be able to evaluate and optimize link performance criteria correctly, a clear definition of the performance metrics is required.

Firstly, the aim is to establish the overall power dissipation for an optical link at a given data rate and BER. The calculation is essentially conditioned by the receiver as explained above, since the BER defines the lower limit for the received optical power. This lower limit can then be used to calculate the required power coupled into waveguides by optical sources, the required detector efficiency (including optical coupling) and acceptable transmission losses. Power

can then be estimated from source bias current and photo-receiver front-end design methodologies.

For interconnect density aspects, source and detector sizes must be taken into account, while the width, pitch and required bend radius of waveguides is fundamental to estimating the size of the photonic layer. On the circuit layer, the additional surface due to optical interconnect is in the driver and receiver circuits, as well as the depassivated link to the photonic layer. The circuit layout problem is compounded by the necessity of using clean supply lines (i.e. separate from digital supplies) to reduce noise (for BER).

The data rate is essentially governed by the bandwidth of the photo-receiver: high modulation speed at the source is generally more easily attainable than similar detection speed at the receiver. This is essentially due to the photodiode parasitic capacitance at the input of the transimpedance amplifier.

The limitations of this analysis as carried out here are that:

- PTM models do not take noise into account particularly well, which means that no real noise analysis can be carried out. However in the sizing process this problem was circumvented by using the Morikuni formula to estimate noise at block level.
- no automatic layout generation tools were used as it is not in general possible to achieve optimal layout for high-speed analog circuits. Parasitic capacitances were therefore extracted from layout estimations rather than from real layouts.

### C. Specifications

Table II shows the sets of specifications used for analysis and interface circuit sizing. Three predictive technologies were considered for this analysis: PTM models [23] for 65nm, 45nm and 32nm gate length technology nodes.

TABLE II  
LINK SPECIFICATION SET

Parameter	Scenario	PTM65	PTM45	PTM32
BER	bits <sup>-1</sup>	10 <sup>-18</sup>	10 <sup>-18</sup>	10 <sup>-18</sup>
ITRS max. frequency	bit/s	2.98 × 10 <sup>9</sup>	5.20 × 10 <sup>9</sup>	1.10 × 10 <sup>10</sup>
Link length	mm	{2.5,20}	{2.5,20}	{2.5,20}
Activity rate		1	1	1
Ambient temperature	°C	70	70	70
Vdd (CMOS)	V	1.2	1.1	1.0

## VI. INTERCONNECT DENSITY ANALYSES

In this work, we supposed that only one photonic routing layer would be available above IC. The impact of this hypothesis is that interconnect links can only be defined in a single routing direction (this does not exclude the occasional use of bends to avoid routing obstacles) due to unacceptable crosstalk (around 10% power loss) for straight waveguide crossings, and unacceptable area penalties (around 10x10μm<sup>2</sup>) for optimized crossings (1% power loss at 1.55μm wavelength) [24].

Direct optical link bundles (Figure 10) were considered to be used for all inter-processor communication, except between physically adjacent processors (electrical buses used in this case). Normally of course, a design engineer would not create

a fully connected architecture, but this is still a useful example to explore and quantify achievable interconnect density.

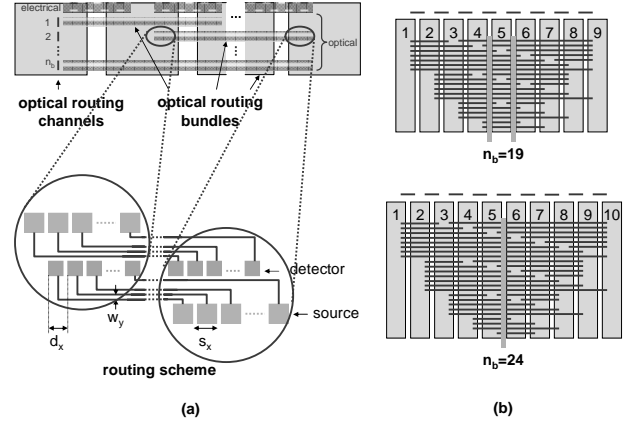


Figure 10 Routing scheme for processor matrix showing (a) organization of routing bundles and channels and detail of source/detector matrices at each end of a bidirectional link, and (b) example routing schemes and optical routing channel count for odd (9) and even (10) IP block number cases

A number of parameters were defined in order to carry out interconnect density analyses, and are summarized in Table III.

TABLE III  
OPTICAL INTERCONNECT ROUTING DENSITY PARAMETERS

p <sub>x</sub>	number of IP blocks in row	{2; 10}
c <sub>x</sub> <td>side of total chip (m)</td> <td>0.02</td>	side of total chip (m)	0.02
s <sub>x</sub> <td>x-direction source pitch (m)</td> <td>{10e-6; 100e-6}</td>	x-direction source pitch (m)	{10e-6; 100e-6}
s <sub>y</sub> <td>y-direction source pitch (m)</td> <td>{10e-6; 100e-6}</td>	y-direction source pitch (m)	{10e-6; 100e-6}
d <sub>x</sub> <td>x-direction detector pitch (m)</td> <td>{10e-6; 100e-6}</td>	x-direction detector pitch (m)	{10e-6; 100e-6}
d <sub>y</sub> <td>y-direction detector pitch (m)</td> <td>{10e-6; 100e-6}</td>	y-direction detector pitch (m)	{10e-6; 100e-6}
w <sub>v</sub> <td>waveguide pitch (m)</td> <td>{1.1e-6; 4e-6}</td>	waveguide pitch (m)	{1.1e-6; 4e-6}
w <sub>b</sub> <td>waveguide bend radius (m)</td> <td>{2e-6; 10e-6}</td>	waveguide bend radius (m)	{2e-6; 10e-6}

If we assume that the overall chip is square, then the total chip size =  $c_x^2$ . If each IP block is also square then the IP block size =  $c_x^2/p_x^2$ . Since the coupling from sources to waveguides and from waveguides to detectors is electromagnetic, we used the routing scheme shown in Figure 10(a) to prevent any waveguide routing below an optoelectronic device and avoid in this way any potential crosstalk issues. If  $s_x \neq d_x$  then using minimum device spacing will result in data skew and should be evaluated or avoided by non-optimal spacing of the smaller device fixing  $s_x' = d_x' = \max(s_x, d_x)$ . This approach will also result in a delay penalty due to longer waveguide lengths.

For a given number  $p_x$  of IP blocks, we can then calculate:

- the number of optical routing channels necessary for total connectivity (excluding adjacent IP block communication which will be carried out by electrical interconnect)
- the maximum number of links in each bundle, based on waveguide pitch and optoelectronic device dimensions

### A. Number of optical bundles

The number of necessary optical routing channels can be calculated by examining the connection scheme between IP

blocks and determining the number of channels at the plane where the maximum connection density occurs. A number of cases can be considered in order to derive a general model for the number of necessary channels, as shown in Figure 10(b). In fact, two basic cases can be extracted: for an even number of IP blocks, a single dense plane exists, whereas for an odd number of IP blocks, two dense planes exist.

In general:

$$n_b = p_x(p_x - 2) - \sum_{i=2}^{p_x-1} i - \sum_{i=2}^{\lfloor \frac{p_x-1}{2} \rfloor} p_x - 2i \quad (8)^3$$

This is shown in graphical form in Figure 11.

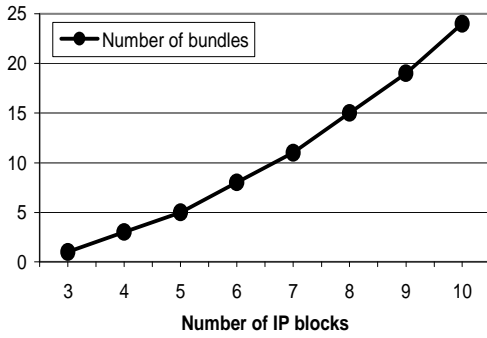


Figure 11 Number of channels for varying number of IP blocks

### B. Number of optical links per bundle

The total number of optical links in a row depends on the side of the total chip  $c_x$ , the number of rows (equal to  $p_x$  if the chip is square and the IP blocks are also square), the pitch between waveguides  $w_y$ , the source and detector pitches ( $s_x$ ,  $s_y$ ,  $d_x$ ,  $d_y$ ) and waveguide bend radius.

The maximum average number of aligned sources or detectors over the width of an IP block,  $n_{sd}$  is calculated as:

$$n_{sd} = \text{floor}\left(\frac{c_x/p_x}{(s_x + d_x)/2}\right) \quad (9)$$

The maximum number of links in a row,  $n_l$  is calculated as:

$$n_l = \text{floor}\left(\frac{c_x/p_x}{\max(s_y, d_y) + 2w_b + n_{sd}w_y}\right) * n_{sd} \quad (10)$$

The maximum number of bi-directional links in a bundle,  $n_{lc}$  is calculated as:

$$n_{lb} = \text{floor}\left[\text{floor}\left(\frac{n_l}{n_b}\right) / 2\right] \quad (11)$$

Figure 12 shows a plot of the maximum achievable number of bi-directional links in a bundle for varying number of IP blocks in a row and varying source/detector sizes using this routing scheme. It can be seen for example that 64-bit, "crosstalk-free" optical communication buses between 8 IP blocks in a single row can only be achieved for source/detector sizes of around  $10 \times 10 \mu\text{m}^2$  and waveguide pitch of  $1.1 \mu\text{m}$ .

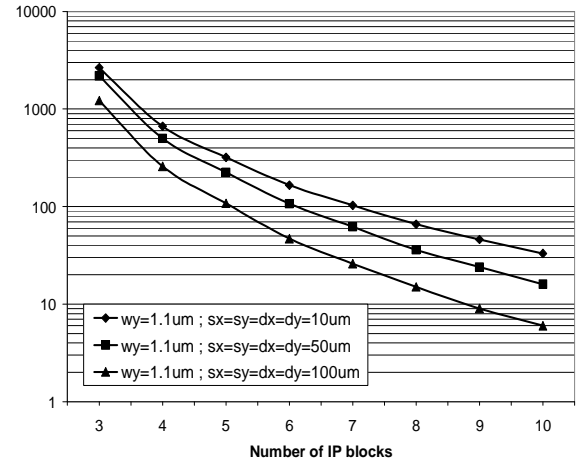


Figure 12 Number of optical links per bundle for varying number of IP blocks (waveguide pitch =  $1.1 \mu\text{m}$ )

### C. Via stack calculations

In order to calculate the area penalty (at the CMOS level) of the via stack for passing a relatively high level of current (mainly driver modulation current to the source), we calculate the via matrix area  $A$ , defined by host technology characteristics and the maximum current passing through the stack. The area required by the via matrix is  $A = N(a+b)^2$ , where  $A$  represents area ( $\mu\text{m}^2$ ),  $N$  represents the number of contacts in the matrix,  $a$  and  $b$  represent minimum contact width ( $\mu\text{m}$ ) and spacing ( $\mu\text{m}$ ), respectively.

The overall surface area of a given metal,  $Na^2$ , is proportional to the maximum current  $I_{\max}$ , following  $N = k_m I_{\max} / a^2$ , where  $k_m$  is a constant associated with the via metal. Rewriting the equation for  $A$ ,

$$A = k_m I_{\max} \left(1 + \frac{b(2a+b)}{a^2}\right) \quad (12)$$

Based on a set of industrial 130nm gate length design rules for which damascene copper is used for all metal layers, we can empirically determine that for the upper-level vias (worst case)  $k_m = 0.466 \mu\text{m}^2/\text{mA}$ .

Even if  $a$  and  $b$  scale with shrinking process rules, it is trivial to show that  $A$  does not scale with the shrinking factor, as long as  $a$  and  $b$  retain the same ratio to each other. In the aforementioned 130nm gate length process,  $a = 0.36 \mu\text{m}$  and  $b = 0.54 \mu\text{m}$  for via5. Hence:

$$A(\mu\text{m}^2) = 2.913 * I_{\max}(\text{mA}) \quad (13)$$

For example, if  $I_{\max}$  is situated at around 5mA, the total via stack area as seen at the circuit level is  $14.56 \mu\text{m}^2$ .

### D. CMOS interface circuit area calculations

In order to validate the area work, the final step is to estimate the real circuit area necessary from gate area sizes. In the absence of satisfactory high-speed analog layout synthesis tools, our approach was to define a skeleton layout<sup>4</sup> based on

<sup>3</sup> floor is the function that rounds a real number to the integer closer to zero

<sup>4</sup> A skeleton layout defines relative positions of transistors, without associating any information concerning actual transistor sizes.

worst case transistor sizes and derive technology-independent layout rules from this. An important consideration in this work is the actual size of the via stack and its position in each interface circuit layout. The resulting estimated layout was used both to calculate circuit area and also to estimate parasitic capacitances on all circuit nodes.

Following transistor-level synthesis of the interface circuits under worst case conditions (65nm technology for 20mm link length, 1.5mA source threshold current and 10% efficiency, 2.7dB/cm waveguide loss, 100fF photodiode capacitance and 50% responsivity), the total gate area of the interface circuits was calculated. The total circuit area was estimated from this using the skeleton layout template shown in Figure 13 (including via stack area) and the lambda rules described in the appendix.

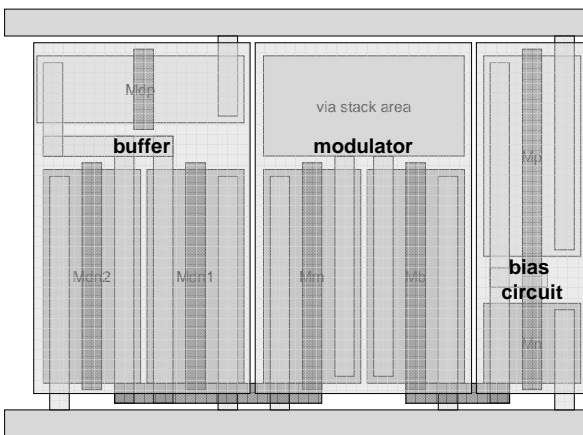


Figure 13 Skeleton layout for current modulation driver circuit

For the receiver circuit, a similar analysis to that of the driver circuit was carried out using the skeleton layout shown in Figure 14 to enable prediction of actual circuit size from transistor gate dimensions.

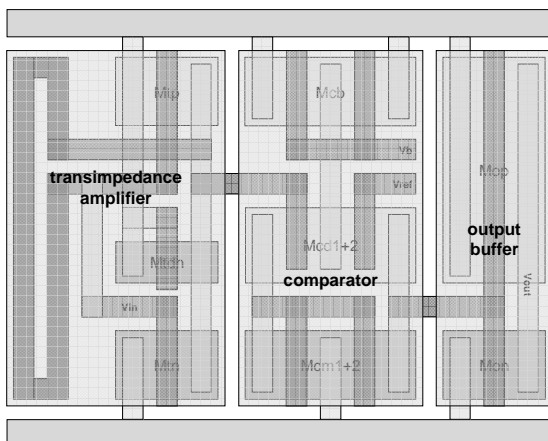


Figure 14 Skeleton layout for receiver circuit

The total area was estimated using this method as  $55.5\mu\text{m}^2$ . This worst case figure for overall CMOS area is considerably

less than the area required for the smallest active device. As such, the active devices remain the limiting factor for area concerns rather than interface circuits.

## VII. INVESTIGATION PROGRAM RESULTS

### A. Gate area analysis for varying technologies

The link sizing method described in section V was applied according to the specifications for the PTM 65nm, 45nm and 32nm technologies. Figure 15 shows the results in terms of gate area (i.e. transistor channel dimensions only), extracted as the sum of all transistor gate channel areas  $W \cdot L$ . These results show that the gate area metric approximately verifies the scaling law ( $A_{32nm} \approx A_{45nm} \cdot s^2 \approx A_{65nm} \cdot s^2 \cdot s^2$ ), where  $s$  is equal to 0.7 (scaling factor between technology generations).

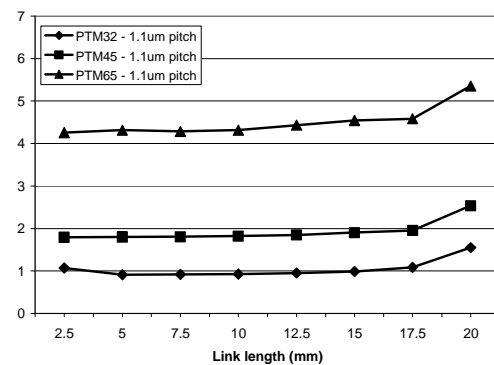


Figure 15 Total CMOS gate area ( $\mu\text{m}^2$ ) for varying optical interconnect length and technologies

### B. Delay analysis

The link sizing method described in section V was applied according to the specifications for the PTM 65nm, 45nm and 32nm technologies. The 50% propagation delay was extracted from simulation, as well as a point of reference in the form of the intrinsic waveguide delay, using  $t_{\text{TOF}}=13.3\text{ps}/\text{mm}$  for the Si/SiO<sub>2</sub> waveguides<sup>5</sup>. Figure 16 shows the delay results for varying link lengths.

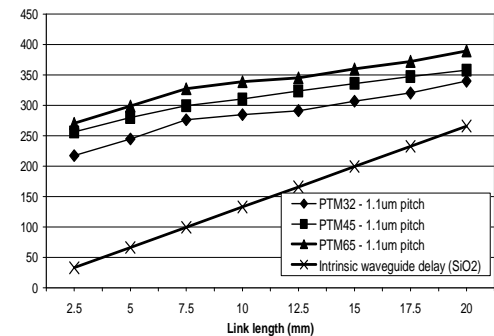


Figure 16 Total link delay (ps) for varying optical interconnect length and technologies

<sup>5</sup> TOF: Time of Flight

It can be seen that a) the *circuit* delay (i.e. the difference between the total delay and the intrinsic waveguide delay) decreases with smaller gate lengths, and b) the same quantity also decreases with longer interconnect. This latter effect is due to higher modulation current  $I_m$ , required to compensate higher overall waveguide loss, being able to drive the source capacitance faster.

C. Power analysis

The link sizing method described in section V was applied according to the specifications for the PTM 65nm, 45nm and 32nm technologies. The average static power was extracted from transient simulations using:

$$\bar{P} = \frac{I_{source_0} + I_{source_1}}{2} \cdot V_p + \frac{I_{det_0} + I_{det_1}}{2} \cdot V_d + \frac{I_{cct_0} + I_{cct_1}}{2} \cdot V_{dd} \quad (14)$$

where  $I_{source}$ ,  $I_{det}$  and  $I_{cct}$  represent the currents flowing through the source, detector and circuit voltage supplies of  $V_p$ ,  $V_d$  and  $V_{dd}$  respectively. Figure 17 shows the average static power results for varying link lengths.

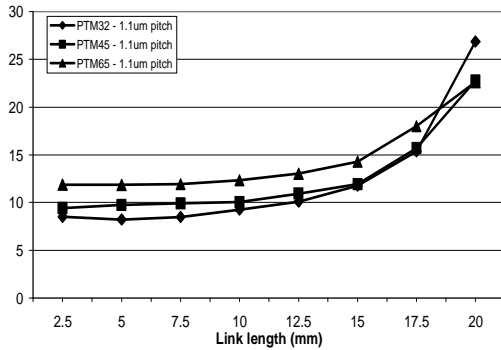


Figure 17 Average static power (in mW) vs interconnect length for PTM 65nm, 45nm and 32nm technologies

The average switching energy is calculated from rising and falling edge transitions (extracted from simulations as the integral of supply currents in edge transitions). Figure 18 shows the average switching energy results for varying link lengths.

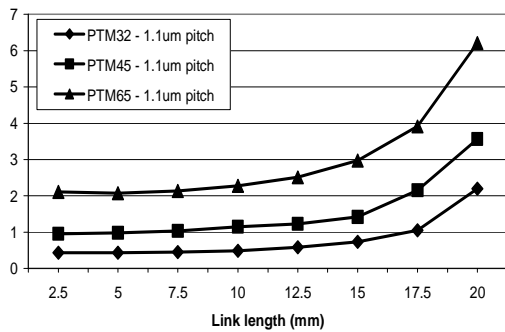


Figure 18 Average switching energy (in pJ) vs interconnect length for PTM 65nm, 45nm and 32nm technologies

Using static power and switching energy information, the total power can be calculated (Figure 19).

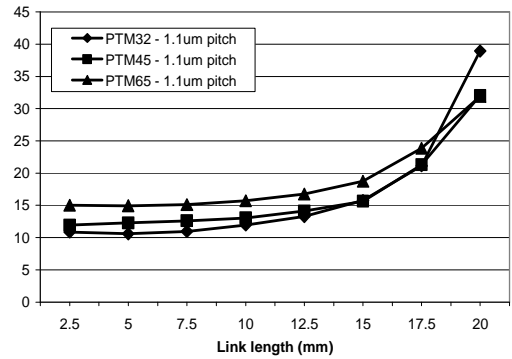


Figure 19 Total power (in mW) vs interconnect length for PTM 65nm, 45nm and 32nm technologies

The figures for aggregated maximum number of links per optical bundle and associated bundle lengths (including additional length due to device staggering) were then used in conjunction with the total power dissipation figures to calculate the total power in one row of interconnected IP blocks, for varying number of IP blocks (from 2 to 10) (Figure 20). It can be seen that the total power decreases with a rising number of IP blocks. This is due to the fact that, while there are more links, each link is shorter. Power increases exponentially with length and is dominated by the source power. For a 10x10 matrix of IP blocks, and for the most long-term technology node (32nm printed gate length), this analysis gives a total power of 33.3W (source threshold currents of 1.5mA). Compared to the figure given by the ITRS for maximum power at this technology node (167W), this works out as equal to 20% of total power.

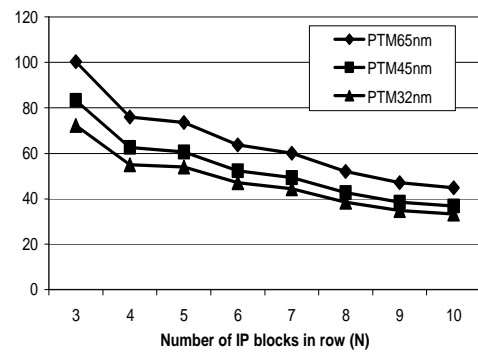


Figure 20 Total power dissipation (W) for varying number of interconnected IP blocks

These results show the capacity of the method to synthesize optical links subject to technological specifications, both CMOS and optical. The generation of each data point requires approximately 5 minutes on a 1.3 GHz processor.

### VIII. DESIGN SPACE EXPLORATION

By carrying out variations on the photonic device characteristic set (within the bounds established in Table I) and rerunning the investigation program, it is possible to establish the impact of individual device characteristics on link performance. This section presents some conclusions from this analysis, as an illustration of the type of feedback our approach can give to photonic device engineers.

#### A. Improvement of waveguide materials

Overall link delay (Figure 21) can be reduced by about a factor of 2 for 20mm interconnect length by shifting to lower index waveguide materials. Interestingly, it can be seen from the figure that the waveguide delay increase for longer lengths is compensated for by faster modulation with higher currents, leading in some cases to a *decrease* in interconnect delay with length. It should be possible, in this configuration, to optimize the system such that overall delay is constant for all interconnect length. This would enable synchronous data communication and reduce dependence on data recovery circuits.

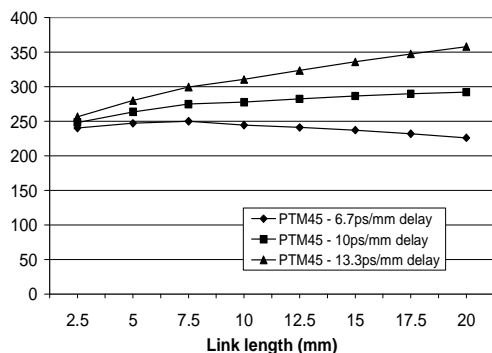


Figure 21 Total link delay (in ps) for varying interconnect length and waveguide intrinsic delay: PTM45nm

#### B. Reduction of source threshold current

Source threshold current has a significant impact on static power (Figure 22). Approximately 5mW can be saved by bringing the threshold current down to 150 $\mu$ A from 1.5mA. While the additional reduction down to 15 $\mu$ A appears negligible in the context of overall link static power, it should be noted that, when multiplied by the total number of links on the chip, even a small individual power saving can represent a significant reduction at the chip scale

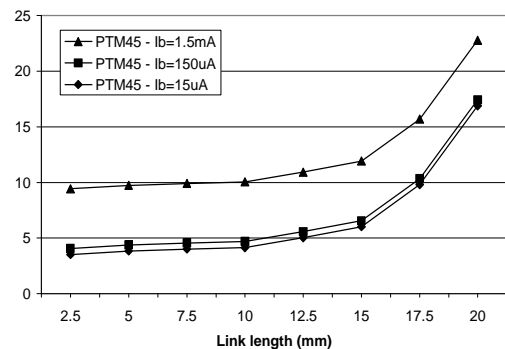


Figure 22 Average static power (mW) for varying interconnect length and source threshold current: PTM45nm

### IX. CONCLUSION

This paper has described a methodology and toolset for the systematic design space exploration of integrated optical interconnect. In particular it allows the automated design of optical links, resulting in a significant reduction in design time and, more importantly in this context, the capacity to carry out a detailed analysis of the available design space. This technology is particularly useful for repetitive design of fixed optical link structures subject to varying design constraints, technology parameters and performance requirements. Further, as designer variability is removed from the overall design process, the resulting set of designs is likely to be relatively coherent and this facilitates interpretation of data and extrapolation to future design scenarios.

We have illustrated the direct application of our approach for link synthesis and technology performance characterization by analyzing optical link performance for a single set of photonic components and three CMOS technology generations. We have also hinted at the ways our toolset can be applied to generate useful feedback from system designers to component designers.

#### APPENDIX: $\lambda$ -RULE SET FOR LAYOUT CALCULATIONS

In a  $\lambda$ -rule layout, all distances and design rules are expressed in so-called  $\lambda$ -units. This means that the layout grid unit is called  $\lambda$ , and it is set to half the minimal gate length ( $\lambda = L/2$ ). All distances are expressed as a number of grid units. If the  $\lambda$ -based design rules are not made too tight, a  $\lambda$ -rule layout can be ported across several technology generations. In this work, the specific design rules used were taken from an existing standard cell library and re-expressed as a function of  $\lambda$ .

For determining the finger widths, we have simplified our calculations by making all fingers equally wide. Hence, we are disregarding finger width restrictions from the layout grid, since we expect this will have very little impact on the simulation results.

As an example of how a scalable  $\lambda$ -rule layout template can be used to estimate layout area, we give a complete illustration for the case of a sample inverter (Figure 23). Table IV

summarizes the design rules and equations that can be used to derive CMOS area estimates.

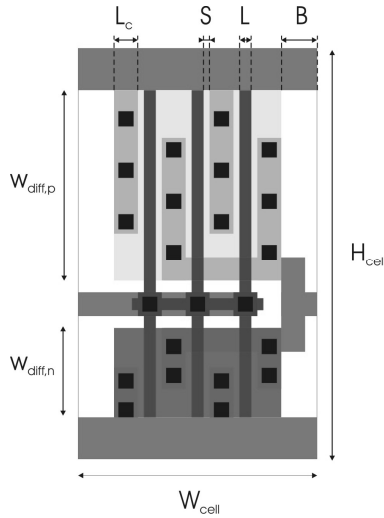


Figure 23: Schematic  $\lambda$ -rule layout used for inverter active area and standard cell area approximations

TABLE IV

SUMMARY OF PSEUDO-LAYOUT PARAMETERS AND EQUATIONS TO DERIVE CMOS CELL AREA ESTIMATES

Symbol	Interpretation	Value or equation
$H_{\text{cell}} (\lambda)$	Standard cell height	69
$W_{\text{a,max}} (\lambda)$	Maximal total active width, i.e. maximal available cell height for MOSFET diffusion regions	47
$W_{\text{n}} (\lambda)$	NMOS gate width, expressed as a multiple of $\lambda$	Set by designer
$W_{\text{p}} (\lambda)$	PMOS gate width, expressed as a multiple of $\lambda$	Set by designer
F	Number of fingers in NMOS and PMOS transistors (equal)	$\text{ceil}((W_{\text{n}}+W_{\text{p}}) / W_{\text{a,max}})$
$W_{\text{diff,n}} (\lambda)$	Width of individual NMOS fingers, set equal to width of NMOS diffusion region.	$W_{\text{n}} / F$
$W_{\text{diff,p}} (\lambda)$	Width of individual PMOS fingers, set equal to width of PMOS diffusion region.	$W_{\text{p}} / F$
L ( $\lambda$ )	MOSFET channel length	2
S ( $\lambda$ )	Spacing between gate poly and metal	1
$L_{\text{c}} (\lambda)$	Width of metal above diffusion region contact	4
B ( $\lambda$ )	Border at right and left edges of cell	6
$L_{\text{diff,ext}} (\lambda)$	Length of MOSFET diffusion region at the edges	$L_{\text{c}} + S = 5$
$L_{\text{diff,int}} (\lambda)$	Per MOSFET length of diffusion region if between fingers	$0.5 (L_{\text{c}} + 2S) = 3$
$L_{\text{diff,tot}} (\lambda)$	Total length of diffusion region (for active area calculation)	$2L_{\text{diff,ext}} + 2(F-1)L_{\text{diff,int}} = 6F - 1$
$L_{\text{act}} (\lambda)$	Total active area length	$L_{\text{diff,tot}} + FL = 8F - 1$
$W_{\text{cell}} (\lambda)$	Standard cell width	$L_{\text{act}} + 2B = 8F + 11$
$A_{\text{gate}} (\lambda^2)$	Total gate area	$FL (W_{\text{diff,n}} + W_{\text{diff,p}}) = 2F (W_{\text{diff,n}} + W_{\text{diff,p}})$
$A_{\text{active}} (\lambda^2)$	Total active area	$L_{\text{act}} (W_{\text{diff,n}} + W_{\text{diff,p}}) = (8F-1)(W_{\text{diff,n}} + W_{\text{diff,p}})$
$A_{\text{cell}} (\lambda^2)$	Total cell area	$W_{\text{cell}} H_{\text{cell}} = 69 W_{\text{cell}}$

## REFERENCES

- [1] J.H. Collet *et al.*, "Architectural approach to the role of optics in mono- and multi-processor machines", *Applied Optics*, 39, 671, 2000
- [2] E.G. Friedman, "Clock distribution networks in synchronous digital integrated circuits", *Proc. IEEE*, 89, 665, 2001
- [3] M. Kobrinsky *et al.*, "On-Chip Optical Interconnects," Intel Technology Journal, vol. 8, no. 2, 2004
- [4] Semiconductor Industry Association, "International Technology Roadmap for Semiconductors," 2005
- [5] J.H. Collet, F. Caignet, F. Sellaye, D. Litaize, "Performance constraints for on chip optical interconnects," *IEEE J. Sel. Top. Quantum Electron.*, vol. 9, no. 2, pp. 425-432, 2003
- [6] P. Rojo-Romeo, J. Van Campenhout, D. Van Thourhout, C. Seassal, P. Regreny, A. Kazmierzczak, C. Seassal, X. Letartre, G. Hollinger, D. Van Thourhout, R. Baets, L. Di Cioccio, J.M. Fedeli, 'Heterogeneous integration of electrically driven microdisk based laser sources for optical interconnects and photonic ICs', *Optics Express*, vol. 14, no. 9, p. 3864, 2006
- [7] A. Sakai, G. Hara and T. Baba, "Propagation Characteristics of Ultrahigh- $\Delta$  Optical Waveguide on Silicon-on-Insulator Substrate", *Jpn. J. Appl. Phys. - Part 2*, vol. 40, no. 383, 2001
- [8] R. Fujita, R. Ushigome, T. Baba, "Continuous wave lasing in GaInAsP microdisk injection laser with threshold current of 40uA," *El. Lett.*, vol. 36, no. 9, p. 790, 2000
- [9] P.R.A. Binetti, X.J.M. Leijtens, M. Nikoufard, R. Orobtcouk, T. Benyattou, T. de Vries, Y.S. Oei, M.K. Smit, "A compact detector for use in photonic interconnections on CMOS ICs," *Proc. Symp. IEEE/LEOS Benelux Chapter*, pp. 233-236, Mons, Belgium, 2005
- [10] J.-M. Fedeli, R. Orobtcouk, C. Seassal, L. Vivien, "Integration issues of a photonic layer on top of a CMOS circuit," *SPIE Photonics Europe*, April 3-7, 2006
- [11] G. Gielen *et al.*, "Analog and Digital Circuit Design in 65nm CMOS: End of the Road?," *Proc. Design Automation and Test in Europe (DATE)*, pp. 36, 2005
- [12] I. O'Connor, F. Tissafi-Drissi, G. Revy, F. Gaffiot, "UML/XML-based approach to hierarchical AMS synthesis", *Proc. Forum on Design Languages*, Lausanne, Suisse, September 27-30 2005
- [13] M. Hamour, R. Saleh, S. Mirabbasi, A. Ivanov, "Analog IP design flow for SoC applications", *Proc. International Symposium on Circuits and Systems (ISCAS)*, p. IV-676, 2003
- [14] S.S. Mohan *et al.*, "Bandwidth extension in CMOS with optimized chip inductors", *IEEE J. Solid-State Circuits*, vol. 35, no. 3, March 2000
- [15] C.W. Kuo *et al.*, "2 Gbit/s transimpedance amplifier fabricated by 0.35 $\mu$ m CMOS technologies", *IEE Electron. Letters*, vol. 37, p. 1158, 2001
- [16] J. Graeme, *Photodiode Amplifiers*, McGraw-Hill, Boston, 1996
- [17] M. Ingels and M.S.J. Steyaert, "A 1-Gb/s, 0.7 $\mu$ m CMOS optical receiver with full rail-to-rail output swing", *IEEE J. Solid-State Circuits*, vol. 34, p. 971, 1999
- [18] I. O'Connor, F. Mieyeville, F. Tissafi-Drissi, G. Tosik, F. Gaffiot, "Predictive Design Space Exploration of Maximum Bandwidth CMOS Photoreceiver Preamplifiers", *Proc. IEEE International Conference on Electronics, Circuits and Systems (ICECS)*, 2003
- [19] E. Kyriakis-Bitaros *et al.*, "Particular aspects of drivers for VCSELs operating at multi-Gb/s", *J. Semiconductor Technol. and Science*, vol. 2, no. 1, pp. 82-86, March 2002
- [20] I. O'Connor *et al.*, "D1.2. Definition and quantification of specifications for different subcomponents", *Deliverable D1.2*, European FP6 Project PICMOS FP6-2002-IST-1-002131, <http://picmos.intec.ugent.be>, March 2006
- [21] C. Seassal *et al.*, "Comparison of proposed architectures for  $\mu$ -source and choice of design to be used for optical link", *Deliverable D3.2*, European FP6 Project PICMOS FP6-2002-IST-1-002131, <http://picmos.intec.ugent.be>, October 2005
- [22] J.J. Morikuni, A. Dharchoudhury, Y. Leblebici, S.M. Kang, "Improvements to the standard theory of photoreceiver noise," *IEEE Journal of Lightwave Technology*, vol. 12, pp. 1174-1184, July 1994
- [23] Y. Cao, T. Sato, D. Sylvester, M. Orshansky, C. Hu, "New paradigm of predictive MOSFET and interconnect modeling for early circuit design," *Proc. Custom Integrated Circuits Conference*, pp. 201-204, 2000
- [24] T. Fukazawa *et al.*, "Low loss intersection of Si photonic wire waveguides", *Jap. J. Appl. Phys.* vol. 43, no. (3), pp. 646-647, 2004